

1       **Radiative forced enhanced semi-arid warming in cold**  
2                                   **season over East Asia**

3                   **X. Guan<sup>1</sup>, J. Huang<sup>1,\*</sup>, R. Guo<sup>1</sup>, H. Yu<sup>1</sup>, P. Lin<sup>2</sup> and Y. Zhang<sup>1</sup>**

4

5

6       <sup>1</sup>Key Laboratory for Semi-Arid Climate Change of the Ministry of Education, College of  
7       Atmospheric Sciences, Lanzhou University, 730000 Lanzhou, China

8       <sup>2</sup> Program in Atmospheric and Oceanic Sciences, Princeton University, 08544 Princeton,  
9       New Jersey, USA

10

11

12

13

14

15

16

17

18

19

20

Submitted to Atmospheric Chemistry and Physics

21

22

23

24

25

26

27

28

---

29       Corresponding author address:

30       Dr. Jianping Huang

31       College of Atmospheric Sciences

32       Lanzhou University,

33       Lanzhou, China, 730000

34       Phone +86 (931) 891-4282

35       E-mail: [hjp@lzu.edu.cn](mailto:hjp@lzu.edu.cn)

36

37 **Abstract**

38 As the climate change occurred over East Asia since 1950s, intense interest and  
39 debate have arisen concerning the contribution of human activities to the warming  
40 observed in previous decades. In this study, we investigate regional surface temperature  
41 change using a recently developed methodology that can successfully identify and  
42 separate the dynamically induced temperature (DIT) and radiatively forced temperature  
43 (RFT) changes in raw surface air temperature (SAT) data. For regional averages, DIT and  
44 RFT make 43.7 and 56.3% contributions to the SAT over East Asia, respectively. The  
45 DIT changes dominate the SAT decadal variability and are mainly determined by internal  
46 climate variability, such as the North Atlantic Oscillation (NAO), Pacific Decadal  
47 Oscillation (PDO), and Atlantic Multi-decadal Oscillation (AMO). The radiatively forced  
48 SAT changes made major contribution to the global-scale warming trend and the  
49 regional-scale enhanced semi-arid warming (ESAW). Such enhanced warming is also  
50 found in radiatively forced daily maximum and minimum SAT. The long-term  
51 global-mean SAT warming trend is mainly related to radiative forcing produced by  
52 global well-mixed greenhouse gases. The regional anthropogenic radiative forcing,  
53 however, caused the enhanced warming in the semi-arid region, which may be closely  
54 associated with local human activities. Finally, the relationship between global warming  
55 hiatus and regional enhanced warming is discussed.

56

57

58

59

60

61

62

63

64

## 65 **1 Introduction**

66 Asia is arguably the most sensitive area to climate change, because it comprises  
67 almost 39% of the world's land area (White and Nackoney, 2003; Huang et al., 2013) and  
68 supports four billion people, which accounts for 66.67% of the world population. A great  
69 portion of its drylands showed a most significantly enhanced warming in the boreal cold  
70 season over mid-to high-latitude areas (Huang et al., 2012). The regional environment  
71 change has a close relationship with local population density and economic development  
72 level. Jiang and Hardee (2011) found that economic growth technological changes and  
73 population growth are the main elements in anthropogenic effects on emission, which  
74 cannot be simulated easily by numerical models (Zhou et al., 2010). More recently, there  
75 are some studies on understanding the implications of population growth, worker  
76 structure and economic intensity for various scenarios of environmental change. The  
77 anthropogenic heating resulting from energy consumption has a significant  
78 continental-scale warming effect in mid-to high-latitudes in winter based on model  
79 simulations (Zhang et al., 2013). The rapid industrialization, urbanization, population  
80 growth, and other anthropogenic activities occurred in East Asia.

81 In the previous studies, dynamic effects induced by greenhouse gases (GHGs) have  
82 been proposed to interpret the rapid warming over continents and non-uniformity of local  
83 warming distribution (Wallace et al., 2012). The dynamic factors exhibit their influences  
84 on surface temperature changes in terms of circulation changes, such as the North  
85 Atlantic Oscillation (NAO), Pacific Decadal Oscillation (PDO), Atlantic Multi-decadal  
86 Oscillation (AMO). Guan et al. (2015) found that the dynamically induced temperature  
87 and radiatively forced temperature had opposite contributions to the surface air  
88 temperature (SAT) during the process of hiatus over the Northern Hemisphere. Most of  
89 the obvious patterns occurred over mid-to high-latitudes where they are known as places  
90 having the earliest warming (Ji et al., 2014) and a phenomenon of enhanced warming  
91 over semi-arid region (enhanced semi-arid warming, ESAW) (Huang et al., 2012). The  
92 ESAW was proposed to be caused by various factors, including changes of atmospheric  
93 circulations, sea surface temperature, interaction between land and atmosphere, feedback  
94 from snow, and so on (Hu and Gao, 1994; Zhang et al., 2001; Huang et al., 2008; Guan et

95 al., 2009; He et al., 2014). But the roles of different factors in the process of ESAW have  
96 not been confirmed.

97 In this study, the roles of different factors in the process of ESAW will be  
98 investigated using a recently developed methodology that can successfully identify and  
99 separate the dynamically induced temperature (DIT) and radiatively forced temperature  
100 (RFT) changes in the raw temperature data. Section 2 introduces the datasets used in this  
101 study. Section 3 provides detailed description of the dynamical adjustment method.  
102 Section 4 shows enhanced warming in semi-arid regions and the behaviors of DIT and  
103 RFT over different regions of East Asia. It analyzes the variability of DIT and the effects  
104 of major natural factors that dominate the dynamic temperature change, and shows the  
105 change of RFT. Section 5 lists all the main findings, followed by some discussion.

## 106 **2 Datasets and study area**

107 This study uses monthly precipitation, monthly mean temperature, monthly daily  
108 maximum and minimum temperature from the land-only TS3.21 dataset obtained from  
109 the Climate Research Unit at the University of East Anglia (Mitchell and Jones, 2005).  
110 The data cover the period of 1901-2012 with a high spatial resolution of  $0.5^\circ \times 0.5^\circ$ . The  
111 regionally-average temperature trend of region  $k$  is calculated using

$$\bar{T}_k = \frac{\sum_{i=1}^{N_k} W_{ki} \times T_{ki}}{\sum_{i=1}^{N_k} W_{ki}} \quad (1)$$

112 where  $N_k$  is the number of grids in region  $k$ ,  $T_{ki}$  is the temperature of grid  $i$  in region  $k$ ,  
113 and  $W_{ki} = \cos(\theta_i \times \pi / 180)$ , with  $\theta_i$  is the latitude of the grid  $i$ . The temperature trend  
114 of region  $k$  is calculated by least square method based on the time series of  $\bar{T}_k$ .

115 The contribution of RFT (DIT) to raw temperature is calculated as formula (2)

$$CR = \frac{1}{n} \sum_{i=1}^n (\tilde{T}_i^2 / T_i^2) \times 100\% \quad (2)$$

118 Where  $n$  is the number of years of temperature dataset,  $\tilde{T}_i$  is the radiatively forced  
119 temperature or dynamically induced temperature of year  $i$ ,  $T_i$  is the raw temperature of  
120 year  $i$ .

121 The study area is between 20°N and 53°N, and between 73°E and 150°E, which  
122 comprises much of East Asia. The distribution of 30-yr averaged annual precipitation  
123 from 1961-1990 (Fig. 1) illustrates most of semi-arid region (annual precipitation  
124 between 200-600 mm $\text{yr}^{-1}$ ) located in the northeast, and most of arid region is in the  
125 northwest area. It exhibits a generally increase pattern of annual precipitation from  
126 Northwest to Southeast. The wet regions are most distributed in the South area. Although  
127 precipitation is related to surface temperature, the long-term mean precipitation is the  
128 simplest index for classifying climate regions (Huang et al., 2012).

### 129 **3 Dynamical adjustment methodology**

130 The dynamical adjustment method was first proposed by Wallace et al. (2012) and  
131 used to analyze non-uniformity of spatial warming over the Northern Hemisphere. The  
132 SAT, or the raw temperature data is divided into two parts by the dynamical adjustment  
133 method: DIT and RFT. Wallace et al. (2012) claimed the dynamical adjustment method  
134 can remove the dynamic component of the SAT induced by atmospheric circulation  
135 pattern from the raw SAT in the cold season (November-March) over land areas  
136 poleward of 20°N.

137 The dynamical adjustment methodology used in this study has been improved by  
138 Smoliak et al., (2015). The exact process of partial least square (PLS) is to derive  
139 monthly dynamical adjustment of Northern Hemisphere land surface temperature field in  
140 a pointwise manner, namely, temperature time series of each grid point is a predictand.  
141 The data of sea level pressure (SLP) are standardized, and the temperature time series are  
142 standardized and high pass filtered prior to carrying out the following dynamical  
143 adjustment steps: (1) correlate the grid-point temperature time series with its  
144 corresponding SLP to generate a one-point cross-correlation map; (2) project the monthly  
145 SLP field onto the correlation pattern, weight each grid point by the cosine of its latitude  
146 to obtain the first PLS predictor time series  $Z_1$ ; (3) regress this PLS predictor  $Z_1$  out of

147 both the each grid-point temperature time series and its SLP predictor field using  
148 conventional least square fitting procedures, which can obtain a residual temperature time  
149 series and residual SLP field. Repeat these steps on the residual temperature time series  
150 and residual SLP field to obtain the respective PLS predictor  $Z_2$  and  $Z_3, \dots, Z_n$ , which are  
151 mutually orthogonal. In our study, the improved dynamical adjustment methodology  
152 (Smoliak et al., 2015) has been applied to the temperature dataset and three predictors are  
153 retained, which are determined by cross-validation.

154 Following the process stated above, the components associated with changes of  
155 atmospheric circulation patterns that are expressed in terms of SLP are partitioned, and  
156 referred to as DIT variability. The rest is the residual part associated with radiatively  
157 forced factors, called the RFT. The RFT is considered as a result of build-up of GHGs,  
158 stratospheric ozone depletion, volcanic eruption, aerosol emission, local anthropogenic  
159 forcing, and so on. For semi-arid region of East Asia we are interested in, non-radiative  
160 factors resulting from thermodynamic processes is also a part of RFT. As their proportion  
161 are small over the semi-arid regions, its effects in RFT are ignored in this study.  
162 Therefore, we can use the dynamical adjustment method to identify the roles of DIT and  
163 RFT in the process of enhanced warming.

#### 164 **4 Results analysis**

165 Figure 2 compares the variation of cold season-mean SAT of raw, dynamically and  
166 radiatively forced temperatures over East Asia in the period of 1902-2011. The curves  
167 exhibit a warming trend in the past century as a whole and an obvious warming from the  
168 1970s to the 1990s. Then, the raw temperature change (black line) appeared a stoppage  
169 since about 2000 until now. The DIT (blue line) exhibits obvious decadal variability, with  
170 a relatively warming period from the 1970s to the 1990s and an obvious cooling period  
171 from 2000 to 2011 in the cold season. The RFT (red line) shows a rapid increasing rate  
172 since the late 1970s, which is consistent with the raw temperature data. The different  
173 evolutions of DIT and RFT indicate that the time series of DIT and RFT had different  
174 roles in the process of raw temperature variability.

175 Figure 3 shows the spatial distribution of raw, DIT and RFT trends over East Asia in  
176 the period of 1902-2011. Figure 3a exhibits a gradually increasing warming pattern from  
177 south to north and a strong warming trend located over northern East Asia, especially in  
178 Mongolia and Northeast China. The rate of warming was less than  $0.005^{\circ}\text{C}/\text{year}$  in the  
179 south of  $40^{\circ}\text{N}$ , with a small scale of cooling region over the southwest. The distribution  
180 of DIT trend (Fig. 3b) shows a basic warming background of East Asia. The warming  
181 rate over most areas was less than  $0.01^{\circ}\text{C}/\text{year}$ , with a higher value in the northern part  
182 than in the southern part as a whole, and a cooling scale was located in the Northeast of  
183 East Asia. The distribution of RFT trend (Fig. 3c) exhibits a similar distribution as that of  
184 the raw temperature. It shows an obvious warming over the northern area, which reached  
185  $0.025^{\circ}\text{C}/\text{year}$  in some regions. A larger scale of cooling located in the southern region  
186 demonstrates that the cooling in the raw temperature was due to the radiative factors. The  
187 difference of DIT trend distribution from RFT indicates that the influence of radiative  
188 forcing on regional temperature changes is much higher than dynamic factor.

189 The discrepancy of distributions between DIT and RFT trends demonstrates the roles  
190 of DIT and RFT were different. Figure 4 gives the distributions of contributions of DIT  
191 and RFT to the raw temperature in the cold season over East Asia in the period of  
192 1902-2011. It exhibits quite different locations of high contribution for DIT and RFT.  
193 The dynamic contribution to the raw temperature change (Fig. 4a) has high values over  
194 the northwest and along the coastal area of Southeast China, but the peak value is much  
195 less than its radiative value. In the spatial distribution of RFT contribution (Fig. 4b), the  
196 positive centres were located over the northeast and southwest areas, and the values were  
197 much higher than those in Fig. 4a. The difference between Fig. 4a and Fig. 4b illustrated  
198 the regional temperature is mainly contributed by RFT. This regional discrepancy is  
199 confirmed by the contributions of DIT (blue line) and RFT (red line) to the raw  
200 temperature as a function of annual precipitation in the cold season over East Asia (Fig.  
201 5). Figure 5 shows that the RFT made a greater contribution than the DIT over the whole  
202 region. The contribution of RFT increased as the annual precipitation increased. Opposite  
203 to the radiative contribution, the dynamical contribution decreased with the increase of  
204 annual precipitation.

205 According to Huang et al. (2012), the enhanced warming occurred over the semi-arid  
206 regions. Figure 6 provides the long-term trends of DIT and RFT as a function of  
207 annual-mean precipitation. It illustrates that the RFT had a major contribution to the  
208 regional variation and showed a similar curve as the raw temperature over different  
209 regions. Both the raw data and RFT reached the peak in the area of 300-400  $\text{mmyr}^{-1}$ . The  
210 fact that the peaks of temperature trend of both raw data and RFT occurred over  
211 semi-arid regions indicates that the radiative factors had dominated roles in the process of  
212 enhanced warming over the semi-arid regions. However, the DIT trend did not show  
213 obvious difference over different areas. It kept a mean rate of  $0.005^{\circ}\text{C}/\text{year}$ , which is far  
214 away from the  $0.017^{\circ}\text{C}/\text{year}$  of the highest value in the drylands of the RFT trend. The  
215 greater warming rate in semi-arid region appeared in both raw temperature and RFT  
216 indicated that enhanced warming occurred in drylands is mainly led by RFT. It  
217 improves the understanding of the ESAW (Huang et al., 2012), and suggests that role of  
218 radiative forced part in the process of warming East Asia.

219 These results are not limited to the monthly-mean temperatures, the daily minimum  
220 and maximum temperatures expressed different variability of DIT and RFT as well.  
221 Figure 7 shows the distributions of raw, dynamically induced and radiatively forced daily  
222 minimum temperature trends over East Asia in the period of 1902-2011. The raw daily  
223 minimum temperature illustrates a similar distribution as the raw monthly-mean  
224 temperature, with a stronger warming trend over northern East Asia, especially over  
225 Mongolia and Northeast China. The dynamically induced daily minimum temperature  
226 (Fig. 7b) shows a warming pattern over most areas, with a small cooling in the area along  
227 the Northeast China. The RFT trend (Fig. 7c) had an obvious warming over the northern  
228 area, with a smaller cooling over South China than in the monthly-mean temperature.

229 Figure 8 is the distributions of raw, dynamically and radiatively of daily maximum  
230 temperature trends over East Asia in the period of 1902-2011. The raw daily maximum  
231 temperature trend (Fig. 8a) had a warming trend over Northern East Asia, especially over  
232 Mongolia. But the warming extent was apparently less than that in the daily minimum  
233 temperature. The cooling in the southern part was larger than that in the daily minimum  
234 temperature. The dynamically induced daily maximum temperature (Fig. 8b) shows a



235 slight warming over most areas, with a cooling located in the area along of Northeast  
236 China. The RFT trend (Fig. 8c) had an obvious warming over the northern area, with a  
237 small cooling scale over South China, which is similar with the raw daily minimum  
238 temperature. But the scale of cooling area was much larger than the radiatively forced  
239 daily minimum temperature in Fig. 7c.

240 In order to distinguish the regionally-averaged temperature changes, the daily  
241 minimum and maximum of raw, DIT and RFT as a function of annual-mean precipitation  
242 are shown in Fig. 9 and Fig. 10, respectively. The daily minimum (Fig. 9) had a higher  
243 warming rate than the daily maximum (Fig. 10) over different regions, especially in the  
244 drylands. The peaks of RFT over the drylands in both daily minimum and maximum  
245 temperatures indicate the dominated roles of radiative effects in the regional warming.  
246 But, the DIT trend did not show a similar variability over different area in both daily  
247 minimum and maximum temperatures. The higher values of RFT of both daily minimum  
248 and maximum temperatures in the drylands emphasize the major roles of RFT in the local  
249 enhanced warming process.

250 The DIT was mainly dominated by major dynamic factors, such as the NAO (Li et  
251 al., 2013), PDO (Trenberth and Hurrell, 1994; Kosaka and Xie, 2013) and AMO (Wyatt  
252 et al., 2012; Wyatt and Curry, 2014). The correlation coefficients between DIT and  
253 NAO/PDO/AMO (Fig. 11) illustrate the influences of these dynamic factors. Figure 11a  
254 shows the distribution of the correlation coefficient between the NAO and the DIT. It  
255 exhibits positive patterns cover most of the East Asia area, with a 95% confidence level  
256 over Mongolia, Inner Mongolia and Northeast China; and negative patterns over India  
257 and Southwest China, with a 95% confidence level. It suggests the strong positive  
258 influence of the NAO on the DIT over the northern area and the negative effect over the  
259 southwest of East Asia. Figure 11b is the correlation coefficient between PDO and DIT.  
260 Only the negative correlation coefficients over boundary of China and India pass the  
261 confidence level of 95%. In South China and North China, there were positive and  
262 negative patterns, respectively. Meanwhile, the negative correlative coefficient of AMO  
263 index and DIT (Fig. 11c) covered the most area of East Asia, except for a small positive

264 region in the southwest of East Asia. The general spatial distribution is opposite with the  
265 distribution of the NAO.

266 The RFT variability is always considered as a result of GHGs, but more climate  
267 effects of aerosols were revealed in the recent decades (Li et al., 2011). The fast  
268 industrialization process over East Asia produced more anthropogenic GHGs and  
269 aerosols, and impacted the local climate change (Qian et al., 2009, 2011). The  
270 temperature of Coupled Model Intercomparison Project Phase 5 (CMIP5) (Taylor et al.,  
271 2012) is always marked with its correspondence to the concentration of the GHGs. In  
272 order to manifest the effects of GHGs in RFT, a comparison between RFT and a  
273 20-model ensemble mean of CMIP5 simulations (Table 1) over the East Asia is plotted  
274 (Fig. 12), which shows that the time series of the CMIP5 simulations are smoother than  
275 the observed SAT curve. But, the notable consistent exists between RFT and simulated  
276 SAT in the warming period from the 1970s to the late 1990. The consistent curve of RFT  
277 and CMIP5 indicated the simulation reflect radiative part of raw temperature.

278 The distributions of correlation coefficients of DIT and RFT with simulated  
279 temperature of CMIP5 are expressed in Fig. 13. Figure 13a exhibits a negative pattern  
280 over most of the area except for the boundary between Northwest China and Russia and  
281 southwest. But in Fig. 13b, the correlation coefficient of RFT with CMIP5 ensemble  
282 mean temperature has a positive pattern over most of China, which passes the 95%  
283 confidence level, excluding the northeast of China and Mongolia. It indicates the  
284 temperature of CMIP5 has a closer relationship with RFT than DIT, namely, CMIP5  
285 models reflect part of raw temperatures. The high positive correlation coefficient between  
286 RFT and ensemble mean of CMIP5 indicates the radiatively forced influence take a  
287 major proportion in simulated temperature change. The ensemble mean temperature trend  
288 as a function of annual precipitation (Fig. 14) highlights the regional RFT over the  
289 drylands (Fig. 6). It illustrates that the enhanced warming over the semi-arid regions led  
290 by the RFT does not appear in the ensemble mean temperature, which demonstrates the  
291 CMIP5 simulations prefer a uniform temperature change over all the regions. The  
292 significant difference between RFT and simulated temperatures over the drylands  
293 indicates that the enhanced warming over semi-arid region was not mainly related to

294 radiative forcing produced in models, such as GHGS, land cover change, aerosol and so  
295 on. It is more related with regional factors not totally considered in the models.

## 296 **5 Summary and discussion**

297 Our results suggest that the enhanced warming in the drylands was induced by the  
298 RFT. The DIT and RFT extracted from the raw temperature had different contributions in  
299 the process of temperature change. For the regionally averaged values, the DIT and RFT  
300 contributed 43.7 and 56.3% to the SAT over East Asia, respectively. The DIT that was  
301 dominated by the NAO, PDO and AMO was on decadal time scales. The RFT changes  
302 were the major contributions to the global-scale warming trend and the regional-scale  
303 enhanced warming in the semi-arid regions. Previous studies (Guan et al., 2015) pointed  
304 out the well mixed GHGs took a continuous warming effect over globe in the radiatively  
305 forced temperature change. The local processes dominated the enhanced warming in the  
306 semi-arid regions. These possible local processes have been listed in Fig. 15.

307 The regional RFT was mainly induced by the interaction among atmosphere, land  
308 surface, snow/ice and frozen ground cover change, and regional human activities. For  
309 example, the drying of sandy or rocky soil by higher temperatures would increase surface  
310 albedo, reflecting more solar radiation back to the space. And the substantially declining  
311 of snow/ice and frozen ground change in the past 30 years, particularly from early spring  
312 through summer (Zhai and Zhou, 1997) may cause the surface temperature to increase in  
313 the cold season via the influence on albedo. The thickness of seasonally frozen ground  
314 has decreased in response to winter warming (Lemke et al., 2007), which will emit more  
315 CO<sub>2</sub> into the atmosphere. The net radiation in the semiarid regions will become a  
316 radiation sink of heat relative to the surrounding regions. Besides, Multiza et al. (2010)  
317 found that local anthropogenic dust aerosols associated with human activities (Huang et  
318 al., 2015) such as agriculture and industrial activity accounted for 43 % of the total dust  
319 burden in the atmosphere. The radiatively forced effect of aerosol maybe another key  
320 process in enhanced warming of semi-arid area. More investigations are needed to  
321 quantify the contribution of different local process.

322 Our results also well explained the co-existence of regional warming and hiatus of the  
323 Northern Hemisphere. The major interpretation of the warming trend slowdown (WTS)

324 claimed that natural variability played an important role in global temperature variability  
325 (Easterling and Wehner, 2009; Wyatt et al., 2012, Wyatt and Curry, 2014; Kosaka and  
326 Xie, 2013). The RFT had a warming contribution offset the cooling effect of DIT, and  
327 result in hiatus over the Northern Hemisphere (Guan et al., 2015). According to the  
328 results of our study, the RFT had made a major contribution to global warming, where  
329 the most obvious warming appeared in the drylands. And we conclude that the long-term  
330 global-mean SAT warming trend was mainly related to the radiative forcing produced by  
331 the global, well mixed GHGs. But, the regional anthropogenic radiative forcing caused  
332 the enhanced warming in the semi-arid regions. Therefore, the hiatus as a phenomenon of  
333 global scale was not in conflict with the regionally enhanced warming in the semi-arid  
334 regions.

335

### 336 **Acknowledgements**

337 This work was supported by the National Science Foundation of China (41305009,  
338 41575006) and the National Basic Research Program of China (2012CB955301), and the  
339 China 111 project (No. B 13045). Fundamental Research Funds for the Central  
340 Universities (lzujbky-2015-2, lzujbky-2015-ct03). The authors acknowledge the World  
341 Climate Research Programme's (WCRP) Working Group on Coupled Modelling  
342 (WGCM), the Global Organization for Earth System Science Portals (GO-ESSP) for  
343 producing the CMIP5 model simulations and making them available for analysis, and the  
344 Climate Explorer for making the NAO, PDO and AMO indices were available to  
345 downloaded (<http://climexp.knmi.nl/>).

346

347

348

349

350

351 **References:**

352 Easterling, D. R. and Wehner, M. F.: Is the climate warming or cooling?, *Geophys. Res.*  
353 *Lett.*, 36, L08706, doi:10.1029/2009GL037810, 2009.

354 Guan, X., Huang, J., Guo, N., Bi, J., and Wang, G.: Variability of soil moisture and its  
355 relationship with surface albedo and soil thermal parameters over the Loess Plateau, *Adv.*  
356 *Atmos. Sci.*, 26, 692-700, 2009.

357 Guan, X., Huang, J., Guo, R., and Lin, P.: The role of dynamically induced variability  
358 in the recent warming trend slowdown over the Northern Hemisphere, *Sci. Rep.*, 5, 12669,  
359 doi:10.1038/srep12669, 2015.

360 He, Y., Huang, J., and Ji, M.: Impact of land–sea thermal contrast on interdecadal  
361 variation in circulation and blocking, *Clim. Dynam.*, 43, 3267-3279, 2014.

362 Hu, Y. and Gao, Y.: Some new understandings of processes at the land surface in arid  
363 area from the HEIFE, *Acta. Meteorol. Sin.*, 52, 285-296, 1994.

364 Huang, J., Zhang, W., Zuo, J., Bi, J., Shi, J., Wang, X., Chang, Z., Huang, Z., Yang, S.,  
365 and Zhang, B.: An overview of the semi-arid climate and environment research  
366 observatory over the Loess Plateau, *Adv. Atmos. Sci.*, 25, 906–921, 2008..

367 Huang, J., Guan, X., and Ji, F.: Enhanced cold-season warming in semi-arid regions,  
368 *Atmos. Chem. Phys.*, 12, 5391-5398, doi:10.5194/acp-12-5391-2012, 2012.

369 Huang, J., Ji, M., Liu, Y., Zhang, L., and Gong, D.: Review of climate change research in  
370 arid and semi-arid regions, *Advances in Climate Change Research*, 9, 9-14, 2013 (in  
371 Chinese).

372 Huang, J., Liu, J., Chen, B., and Nasiri, S.: Detection of anthropogenic dust using  
373 CALIPSO lidar measurements, *Atmos. Chem. Phys. Discuss.*, 15, 10163–10198,  
374 doi:10.5194/acpd-15-10163-2015, 2015.

375 Ji, F., Wu, Z., Huang, J., and Chassignet, E. P.: Evolution of land surface air temperature  
376 trend, *Nature Clim. Change*, 4, 462-466, 2014.

377 Jiang, L. and Hardee, K.: How do recent population trends matter to climate change?,  
378 *Popul. Res. Policy. Rev.*, 30, 287-312, 2011.

379 Kosaka, Y. and Xie, S. P.: Recent global-warming hiatus tied to equatorial Pacific surface  
380 cooling, *Nature*, 501, 403-407, 2013.

381 Lemke, P., Ren, J., Alley, R. B., Allison, I., Carrasco, J., Flato, G., Fujii, Y., Kaser, G.,  
382 Mote, P., Thomas, R. H., and Zhang, T.: Observations: changes in snow, ice and frozen  
383 ground, in: *Climate change : the physical science basis. Contribution of Working Group I*  
384 *to the fourth assessment report of the Intergovernmental Panel on Climate Change*, edited  
385 by: Solomon, S., Qin, D., Manning, M., Chen, Z., Marquis, M., Averyt, K. B., Tignor, M.,  
386 and Miller, H. L., Cambridge University Press, Cambridge, United Kingdom and New  
387 York, NY, USA, 372–374, 2007.

388 Li, J. P., Sun, C., and Jin, F. F.: NAO implicated as a predictor of Northern Hemisphere  
389 mean temperature multidecadal variability, *Geophys. Res. Lett.*, 40, 5497-5502, 2013.

390 Li, Z., Niu, F., Fan, J., Liu, Y., Rosenfeld, D., and Ding, Y.: Long-term impacts of  
391 aerosols on the vertical development of clouds and precipitation, *Nat. Geosci.*, 4, 888-894,  
392 doi: 10.1038/NGEO1313, 2011.

393 Mitchell, T. D. and Jones, P. D.: An improved method of constructing a database of  
394 monthly climate observations and associated high-resolution grids, *Int. J. Climatol.*, 25,  
395 693-712, 2005.

396 Mulitza, S., Heslop, D., Pittauerova, D., Fischer, H. W., Meyer, I., Stuut, J. B., Zabel, M.,  
397 Mollenhauer, G., Collins, J. A., and Kuhnert, H.: Increase in African dust flux at the  
398 onset of commercial agriculture in the Sahel region, *Nature*, 466, 226-228, 2010.

399 Qian, Y., Gustafson Jr, W. I., Leung, L. R., and Ghan, S. J.: Effects of soot-induced snow  
400 albedo change on snowpack and hydrological cycle in western United States based on  
401 Weather Research and Forecasting chemistry and regional climate simulations, *J.*  
402 *Geophys. Res.*, 114, D03108, doi:10.1029/2008JD011039, 2009.

403 Qian, Y., Flanner, M., Leung, L., and Wang, W.: Sensitivity studies on the impacts of  
404 Tibetan Plateau snowpack pollution on the Asian hydrological cycle and monsoon  
405 climate, *Atmos. Chem. Phys.*, 11, 1929-1948, doi:10.5194/acp-11-1929-2011, 2011.

406 Smoliak, B. V., Wallace, J. M., Lin, P., and Fu, Q.: Dynamical adjustment of the  
407 Northern Hemisphere surface air temperature field: methodology and application to  
408 observations, *J. Climate*, 28, 1613–1629, 2015.

409 Taylor, K. E., Stouffer, R. J., and Meehl, G. A.: An overview of CMIP5 and the  
410 experiment design, *Bull. Am. Meteorol. Soc.*, 4, 485-498, 2012.

411 Trenberth, K. E., and Hurrell, J. W.: Decadal atmosphere-ocean variations in the Pacific,  
412 *Clim. Dynam.*, 9, 303-319, 1994.

413 Wallace, J. M., Fu, Q., Smoliak, B. V., Lin, P., and Johanson, C. M.: Simulated versus  
414 observed patterns of warming over the extratropical Northern Hemisphere continents  
415 during the cold season, *Proc. Natl. Acad. Sci.*, 109, 14337-14342, 2012.

416 White, R. P. and Nackoney, J.: Drylands, people, and ecosystem goods and services: a  
417 web-based geospatial analysis (PDF version), World Resources Institute (available at:  
418 <http://pdf.wri.org/drylands.pdf> accessed on 30 January 2012), 2003.

419 Wyatt, M. G. and Curry, J. A.: Role for Eurasian Arctic shelf sea ice in a secularly  
420 varying hemispheric climate signal during the 20th century, *Clim. Dynam.*, 42,  
421 2763-2782, 2014.

422 Wyatt, M. G., Kravtsov, S., and Tsonis, A. A.: Atlantic multidecadal Oscillation and  
423 Northern Hemisphere's climate variability, *Clim. Dynam.*, 38, 929-949, 2012.

424 Zhai, P. and Zhou, Q.: The change of northern hemisphere snow cover and its impact on  
425 summer rainfalls in China, *Quarterly Journal of Applied Meteorology*, 8, 231-235, 1997  
426 (in Chinese).

427 Zhang, G., Cai, M., and Hu, A.: Energy consumption and the unexplained winter  
428 warming over northern Asia and North America, *Nature Clim. Change*, 3, 466-470, 2013.

429 Zhang, Q., Wei, G., and Huang, R.: Observation and study of atmospheric drag  
430 coefficients in Dunhuang, *Sci. China Ser. D.*, 31, 783-792, 2001 (in Chinese).

431 Zhou, L., Dickinson, R. E., Dai, A., and Dirmeyer, P.: Detection and attribution of  
432 anthropogenic forcing to diurnal temperature range changes from 1950 to 1999:

433 comparing multi-model simulations with observations, *Clim. Dynam.*, 35, 1289-1307,  
434 2010.

435

436

437

438

439

440

441

442

443

444

445

446

447

448

449

450

451

452

453

454

455

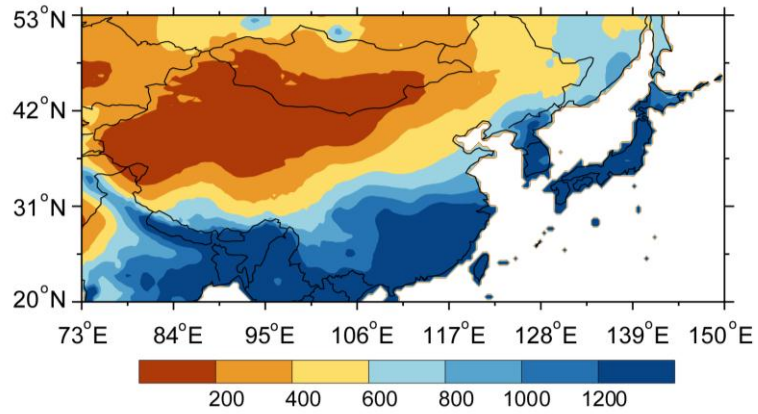
456

457

458

459





460

461

462 **Figure 1.** Spatial distribution of annual mean precipitation from 1961-1990 ( $\text{mm yr}^{-1}$ )

463

464

465

466

467

468

469

470

471

472

473

474

475

476

477

478

479

480

481

482

483

484

485

486

487

488

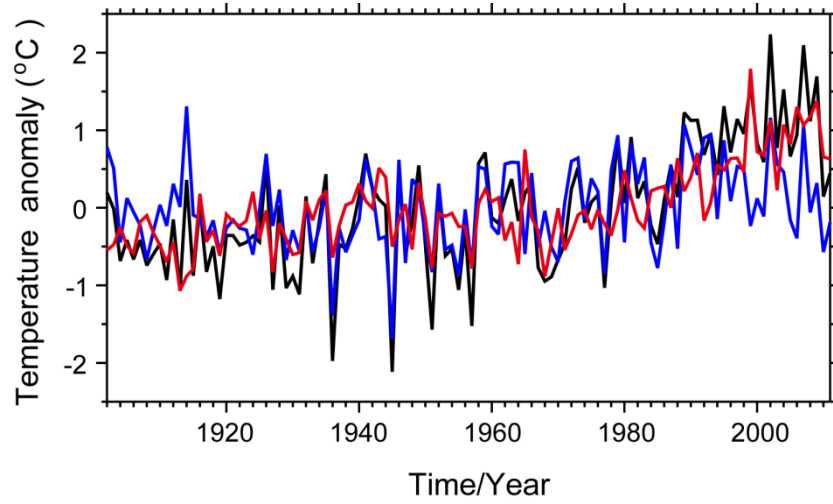
489

490

491

492

493



494

495

496 **Figure 2.** Time series of regionally averaged temperature anomalies of raw (black),  
497 dynamically induced (blue) and radiatively forced (red) temperatures in the cold season  
498 (November to March) from 1902 to 2011 over East Asia.

499

500

501

502

503

504

505

506

507

508

509

510

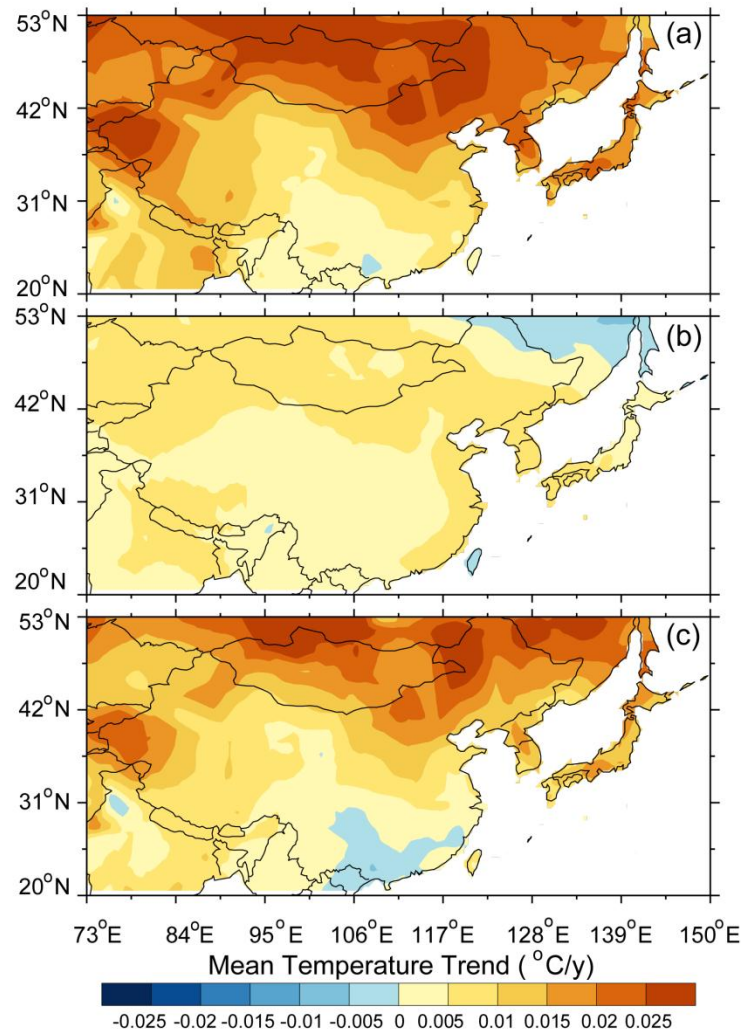
511

512

513

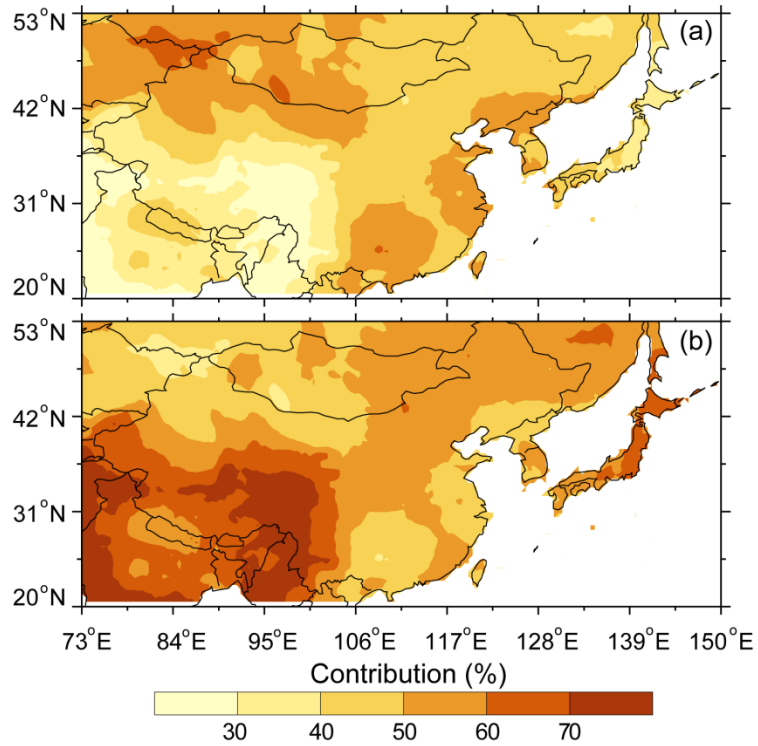
514

515



516  
517

518 **Figure 3.** Spatial distribution of trend of raw (a), dynamically induced (b) and radiatively  
519 forced (c) temperatures in the cold season from 1902 to 2011 over East Asia.



520

521 **Figure 4.** Spatial distribution of contribution of dynamically induced (a) and radiatively  
522 forced (b) temperatures to raw temperature in the cold season from 1902 to 2011 over  
523 East Asia.

524

525

526

527

528

529

530

531

532

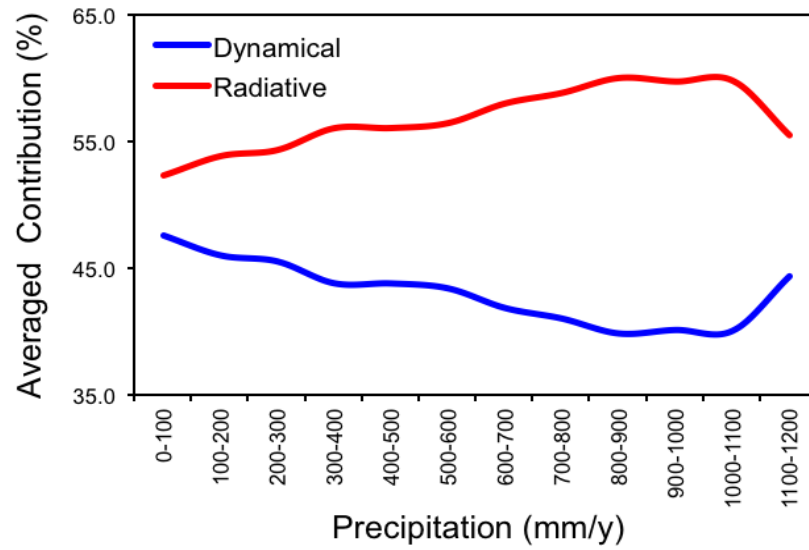
533

534

535

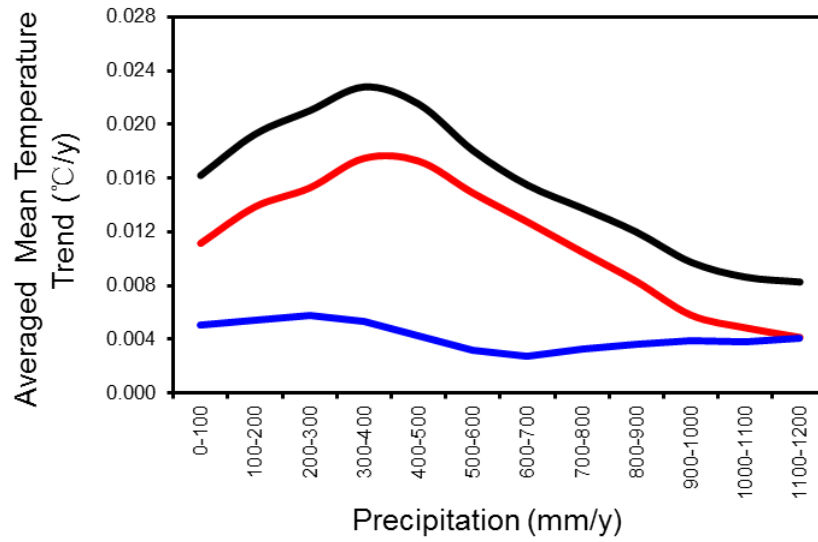
536

537



538  
 539  
 540  
 541  
 542  
 543  
 544  
 545  
 546  
 547  
 548  
 549  
 550  
 551  
 552  
 553  
 554  
 555

**Figure 5.** Contributions of dynamically induced (blue) and radiatively forced (red) temperatures to the raw temperature as a function of annual precipitation in the cold season from 1902 to 2011 over East Asia.



556

557 **Figure 6.** Regionally averaged temperature trend as a function of annual precipitation for  
 558 raw (black), dynamically induced (blue) and radiatively forced (red) temperatures in the  
 559 cold season from 1902 to 2011 over East Asia.

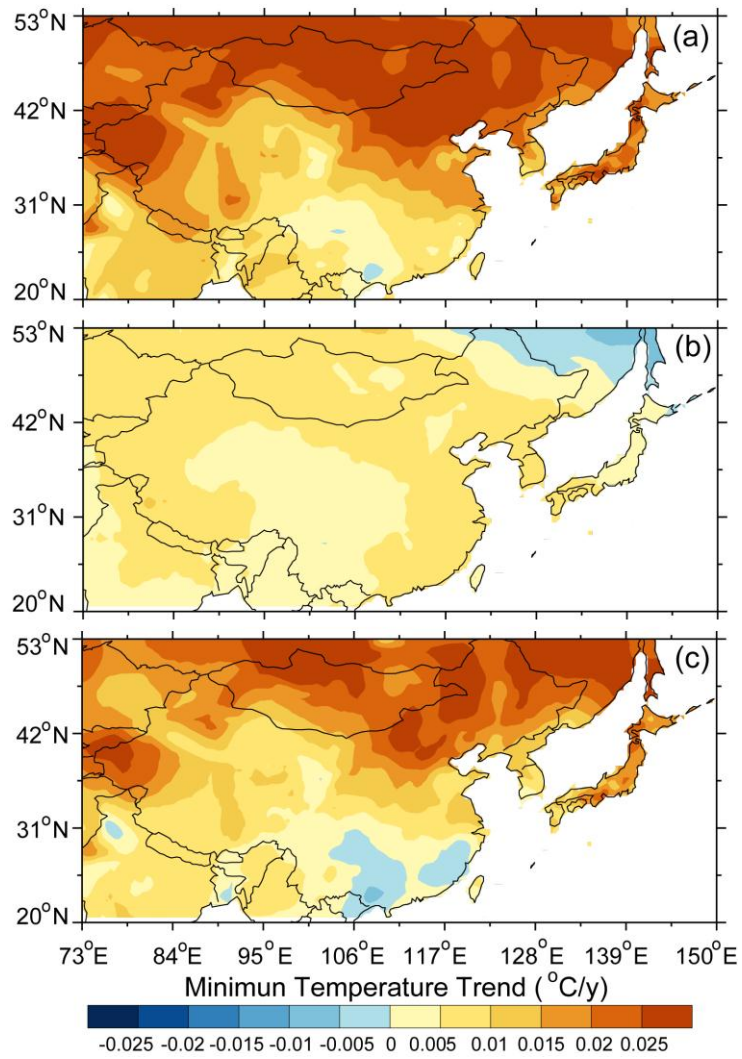
560

561

562

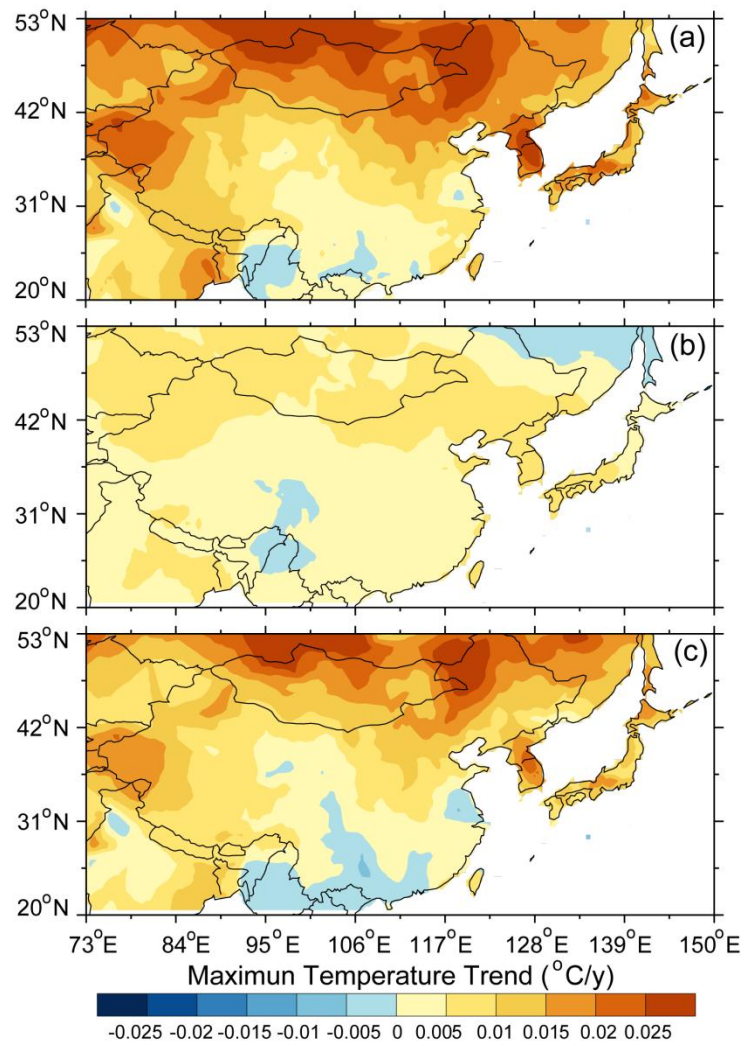
563

564



565  
 566  
 567  
 568

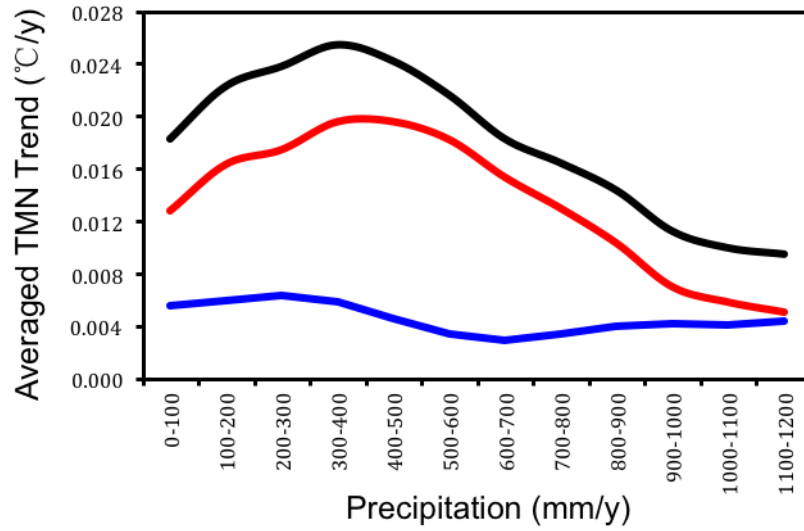
**Figure 7.** Same as Fig. 3, except for daily minimum temperatures.



569  
570  
571  
572  
573  
574  
575  
576  
577  
578  
579  
580  
581

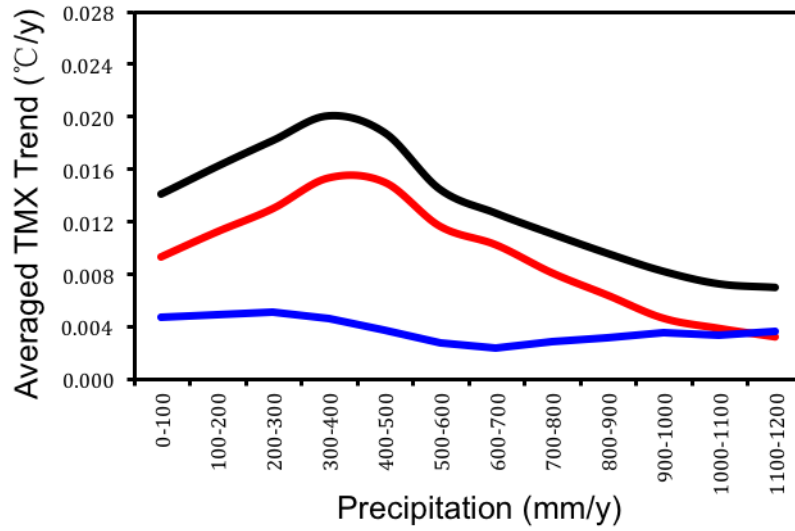
**Figure 8.** Same as Fig. 3, except for daily maximum temperatures.





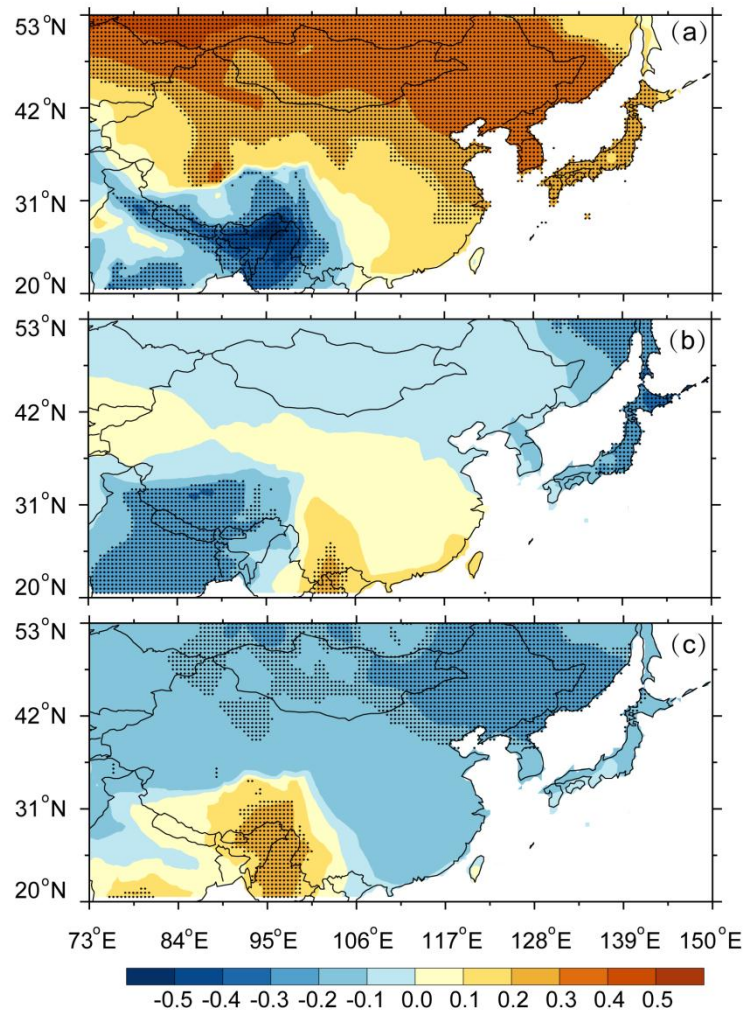
582  
583  
584  
585  
586  
587  
588  
589  
590  
591  
592  
593  
594  
595  
596  
597  
598  
599  
600  
601

**Figure 9.** Same as Fig. 6, except for daily minimum temperature.



602  
603  
604  
605  
606  
607  
608  
609  
610  
611  
612  
613  
614  
615  
616  
617  
618  
619

**Figure 10.** Same as Fig. 6, except for daily maximum temperature.



620  
621

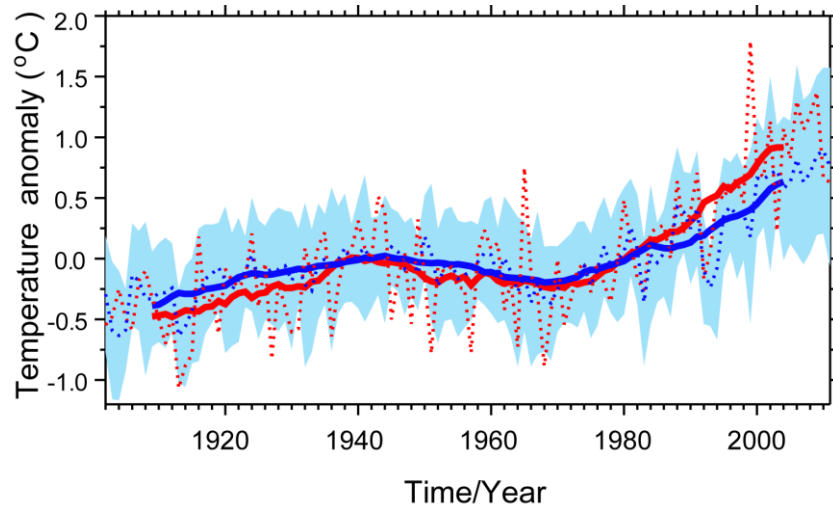
622 **Figure 11.** Spatial distribution of the correlation coefficient between detrended  
623 dynamically induced temperature and detrended NAO (a), PDO (b), and AMO (c) in the  
624 cold season from 1902 to 2011 over East Asia. The stippling indicates the 95%  
625 confidence level according to a two-tailed Student's  $t$  test.

626

627

628

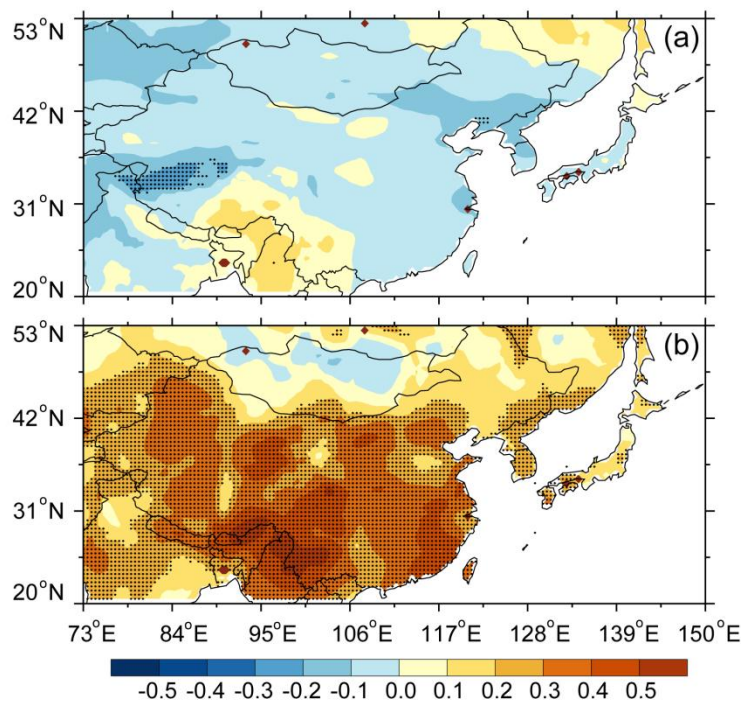
629



630  
631

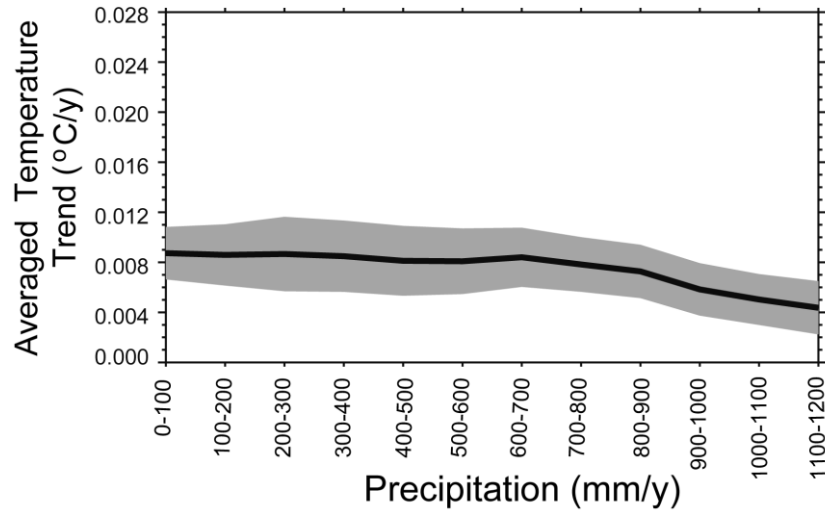
632 **Figure 12.** Time series of radiatively forced temperature (red) and ensemble-mean  
633 CMIP5 simulations (blue) based on 15-yr running mean in the cold season from 1902 to  
634 2011 over East Asia. The blue shading indicates the standard deviation of the  
635 CMIP5-simulated field.

636  
637  
638  
639  
640  
641  
642  
643  
644  
645  
646  
647



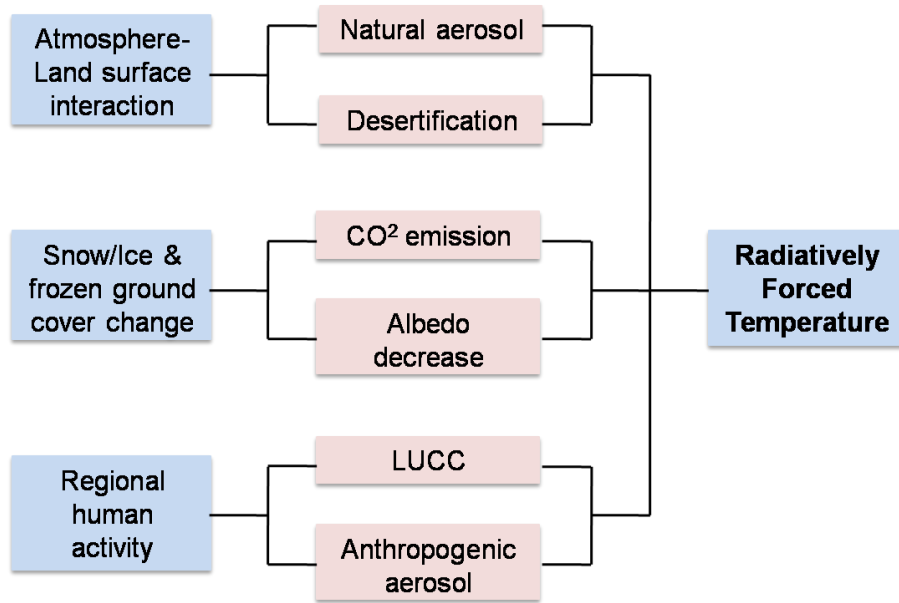
648  
 649  
 650  
 651  
 652  
 653  
 654  
 655  
 656  
 657  
 658  
 659  
 660  
 661  
 662  
 663  
 664  
 665  
 666

**Figure 13.** Spatial distribution of correlation coefficient between ensemble-mean CMIP5 simulations and dynamically induced temperature (a), and between ensemble-mean CMIP5 simulations and radiatively forced temperature (b) in the cold season from 1902 to 2011 over East Asia.



667  
668  
669  
670  
671  
672  
673  
674  
675  
676  
677  
678  
679  
680  
681  
682  
683

**Figure 14.** Regional averaged temperature trend as a function of climatological annual mean precipitation over East Asia for ensemble-mean CMIP5 simulations in cold season from 1902 to 2011, shading denotes 95% confidence intervals.



684  
 685  
 686  
 687  
 688  
 689  
 690  
 691  
 692  
 693  
 694  
 695  
 696  
 697  
 698  
 699  
 700  
 701  
 702  
 703  
 704  
 705  
 706  
 707  
 708  
 709  
 710  
 711  
 712  
 713

**Figure 15.** Schematic diagram of radiatively forced temperature.

714  
715  
716

Table 1. CMIP5 models examined in this study.

Model name	Modelling centre
BCC-CSM1.1	Beijing Climate Center, China
CanESM2	Canadian Centre for Climate, Canada
CanESM2	Canadian Centre for Climate, Canada
CCSM4	National Center for Atmospheric Research, USA
CNRM-CM5	Centre National de Recherches Meteorologiques, France
CSIRO-Mk3.6.0	Commonwealth Scientific and Industrial Research, Australia
GFDL-CM3	Geophysical Fluid Dynamics Laboratory, USA
GFDL-ESM2G	Geophysical Fluid Dynamics Laboratory, USA
GFDL-ESM2M	Geophysical Fluid Dynamics Laboratory, USA
GISS-E2-R	NASA Goddard Institute for Space Studies, USA
HadGEM2-CC	Met Office Hadley Centre, UK
HadGEM2-ES	Met Office Hadley Centre, UK
INM-CM4	Institute for Numerical Mathematics, Russia
IPSL-CM5A-LR	Institute Pierre-Simon Laplace, France
IPSL-CM5A-MR	Institute Pierre-Simon Laplace, France
MIROC-ESM	Japan Agency for Marine-Earth Science and Technology, Japan
MIROC-ESM-CH	Japan Agency for Marine-Earth Science and Technology, Japan
MIROC5	Atmosphere and Ocean Research Institute, Japan
MPI-ESM-LR	Max Planck Institute for Meteorology, Germany
MRI-CGCM3	Meteorological Research Institute, Japan
NorESM1-M	Norwegian Climate Centre, Norway

717  
718  
719  
720  
721  
722  
723  
724  
725